Quantum Mechanical Modeling of Catalytic Processes

Alexis T. Bell[1] and Martin Head-Gordon[2]

[1]Department of Chemical and Biomolecular Engineering, [2]Department of Chemistry, University of California, Berkeley, California 94720; email: bell@cchem.berkeley.edu, m_headgordon@berkeley.edu

Annu. Rev. Chem. Biomol. Eng. 2011. 2:453–77

First published online as a Review in Advance on March 23, 2011

The *Annual Review of Chemical and Biomolecular Engineering* is online at chembioeng.annualreviews.org

This article's doi: 10.1146/annurev-chembioeng-061010-114108

1947-5438/11/0715-0453$20.00

Keywords

catalysis, quantum mechanics, density functional theory, thermodynamics, kinetics

Abstract

Advances in quantum chemical methods in combination with exponential growth in the computational speed of computers have enabled researchers in the field of catalysis to apply electronic structure calculations to a wide variety of increasingly complex problems. Such calculations provide insights into why and how changes in the composition and structure of catalytically active sites affect their activity and selectivity for targeted reactions. The aim of this review is to survey the recent advances in the methods used to make quantum chemical calculations and to define transition states as well as to illustrate the application of these methods to a selected series of examples taken from the authors' recent work.

INTRODUCTION

A long-standing goal in the field of heterogeneous catalysis has been to predict from first principles (*a*) the effects of catalyst composition and structure on the rates of catalyzed reactions as well as (*b*) the distribution of the products formed from a specified set of reactants. Impressive progress toward this end has been made during the past two decades, resulting in a much better understanding of the factors controlling the rates of catalyzed reactions and the influence of catalyst composition and structure on the kinetics of individual elementary reactions. These achievements have resulted from advances in the accuracy and efficiency of electronic structure calculations, particularly those based on density functional theory (DFT), and advances in transition-state-finding algorithms capable of handling large, complex systems. Further contributing to these advances have been improvements in computer speed, memory, and architecture, all of which have resulted in significant reductions in computational time.

This review begins with a survey of advances made in the development of quantum chemical models that have made it possible to describe systems involving tens to hundreds of atoms with increasing speed and accuracy. The development of robust and efficient methods for identification of reaction pathways as well as finding transition states and rate parameters are also surveyed. Four illustrations chosen from the authors' work are then discussed to demonstrate the chemical insights that can be obtained from quantum chemical calculations and the accuracy of these results versus those from experimental observation. We conclude by identifying several challenges for future research that will enable the analysis and simulation of systems more complex than those described here.

QUANTUM MECHANICAL MODELS

Since its discovery, quantum mechanics has been appreciated for providing a first-principles description of the behavior of electrons in molecules. For example, G.N. Lewis (1, p. 18) stated only a decade or so after the development of his electron pair model, "in the Schrodinger equation we very nearly have the mathematical foundation for the solution of the whole problem of atomic and molecular structure." However, Lewis cautioned that "the problem of the many bodies contained in the atom and the molecule cannot be completely solved without a great further development in mathematical technique" (p. 18).

Two critical developments over the past several decades have brought quantum chemistry to the level of maturity and feasibility (2) where it can often be used with great success to identify the relative energies of both stable species (local minima on the potential energy surface) and transition states (saddle points) associated with catalytic processes. The first is exponential growth in computing capabilities, which is associated with a doubling period of approximately 1.5 years such that the capabilities available to a research group in 2010 are approximately 100 times greater than those available in 2000 and are more than 10,000 times greater than those in 1990. The second is the development of robust quantum mechanical models that are both efficient enough to be applied to systems on the scale of 20–200 atoms using present-day computer resources and at the same time accurate enough to provide results that have predictive value. This part of our review summarizes the status of these models, including both their strengths and their limitations.

The prescription of a quantum mechanical model (3) for describing catalysis involves the following three components:

1. **A prescription for the electron-electron interactions**. Direct, brute-force solution of the Schrodinger equation scales exponentially with the number of electrons; therefore, approximations are imperative. The leading approximations are based on DFT and are discussed in

this section. Alternative methods based on model wave functions are available and, although typically more computationally demanding, have the virtue of systematic improvability, which is not necessarily present in DFT.

2. **An expansion basis to represent one-electron functions**. Popular basis sets use either localized atomic orbitals, which are a compact representation for molecules because of their correctness for atoms, or plane waves, which are natural for periodic extended structures. Space limits preclude a detailed discussion of basis sets, but we comment briefly on cost versus accuracy of atomic-orbital basis sets.
3. **A description of the extended environment**. Catalysis takes place in mesoporous solids, on surfaces with diverse adsorbates and in solution with the participation of solvent. A full description of the environment is usually not possible, and the approximations that are made (either a cluster model of the active site, an idealized periodic system, or a simplified model of solvent) will affect the fidelity of the calculation. More details on this aspect of modeling emerge through the specific case studies that are discussed below.

DFT begins from the Hohenberg-Kohn theorems (4). Using the variational principle, it can be established (5) that the ground-state energy of an n-electron system is a functional of only the electron density:

$$E_0 = \min_{\Psi} \langle \Psi | \hat{T} + \hat{V}_{ee} + \hat{V}_{ext} | \Psi \rangle = \min_{\rho} \left\{ \min_{\Psi \to \rho} \langle \Psi | \hat{T} + \hat{V}_{ee} | \Psi \rangle + \int d\mathbf{r} V_{ext}(\mathbf{r}) \rho(\mathbf{r}) \right\}$$
$$= \min_{\rho} \left\{ E_J + E_{T+XC}[\rho(\mathbf{r})] + \int d\mathbf{r} V_{ext}(\mathbf{r}) \rho(\mathbf{r}) \right\}. \quad 1.$$

Equation 1 treats the electron-electron interactions as the classical Coulomb self-repulsion of the density, E_J, plus the quantum effects due to exchange (X) and correlation (C). The unknown universal functional describing kinetic energy and electron-electron interactions (exchange + correlation; XC) must be modeled because its implicit form in the equation above requires knowledge of all n-electron wave functions. The contribution with the largest magnitude, the kinetic energy, has not yet been modeled with high enough precision to be useful for systems other than simple metals (6).

Therefore, an elegant sidestep proposed by Kohn & Sham (7) is used to reintroduce a reference wave function, $|\Psi_S\rangle$, for noninteracting electrons whose density is constructed to be identical to that of the interacting system. The wave function for noninteracting electrons is a simple determinant of one-electron orbitals, the Kohn-Sham molecular orbitals: $|\Psi_S\rangle = \det[\phi_1 \phi_2 \cdots \phi_n]$. It is employed to evaluate the kinetic energy and to parameterize the electron density. The total energy in the resulting Kohn-Sham DFT is

$$E_0 = \min_{\Psi_s} \left\{ \langle \Psi_s | \hat{T} | \Psi_s \rangle + E_J + E_{XC}[\rho(\mathbf{r})] + \int d\mathbf{r} V_{ext}(\mathbf{r}) \rho(\mathbf{r}) \right\}. \quad 2.$$

The XC functional must be modeled. This is the principal challenge for modern DFT, and great progress has been made on this problem (8), though the functionals we describe below still have significant limitations for some classes of problems.

Local Spin-Density Approximation

The simplest exchange and correlation functionals exactly describe a system in which the density is constant rather than being a function of position, i.e., a uniform electron gas (UEG). This defines the local spin-density approximation (LSDA) (7), where the XC functional depends on the spin densities, $\rho_\alpha(\mathbf{r})$ and $\rho_\beta(\mathbf{r})$, which are allowed to be different. The LSDA, although exact for the

UEG and useful for many metals, tends to overbind molecules almost as much (roughly 0.5 eV per pair of electrons) as mean-field Hartree-Fock theory underbinds them. Nevertheless, correctness for the UEG is a virtue that should be retained by more advanced functionals.

Generalized Gradient Approximations

Generalized gradient approximations (GGAs) allow the functional to depend on the gradients of the electron density or the dimensionless, reduced spin-density gradient in addition to the density itself. GGAs are described as "semilocal" functionals because they allow the XC functionals to respond to the way the density is changing. For most chemical applications, popular GGAs such as PBE (9) or BLYP (10, 11) dramatically reduce the large errors associated with the LSDA. They are nearly as computationally efficient as the LSDA and, when using plane-wave basis sets, are much more efficient than the hybrids discussed below.

Hybrid Density Functionals

Hybrid density functionals (12) model a fraction of exchange using the Kohn-Sham reference wave function [for instance, 20% in the B3LYP functional (12, 13), which has been the most successful of the hybrids]. There is a significant improvement in accuracy over the GGAs; therefore, hybrids have become the density functionals of choice. Although the exchange functional now depends on the orbitals, rather than just the density, and is thus outside of the original Kohn-Sham framework, it can be considered a valid "generalized" Kohn-Sham density functional (14).

Although these three levels of DFT are relatively well established, only over the past several years, has it become clear that new functionals of similar cost can produce significant improvements in cases where the performance of common hybrid functionals is most problematical. A separate review is needed to discuss the failures of existing density functionals in detail. However, we here mention the three principal sources of error:

1. **Self-interaction errors**. Because the classical Coulomb energy, E_J, includes the energy of an electron interacting with itself, this must be cancelled by the exchange functional. Failure to fully accomplish the cancellation is termed a self-interaction error (15). It leads to a variety of undesirable artifacts such as incorrect dissociation to fragments with fractional numbers of electrons (16) and, in general, a tendency to favor more delocalized electronic structures [such as transition states (17)]. A larger fraction of exact exchange reduces self-interaction, as 100% cancels it completely. Alternatively, reduction in self-interaction error can also be accomplished by "range separation" of the Coulomb operator (18) for purposes of treating exchange interactions, $1/r = s(r) + l(r)/r$. A partition of unity is introduced so that the short-range part of exchange, most commonly modeled with $s(r) = \mathrm{erfc}(\omega r)$, can be treated by DFT (19), and the corresponding long-range part of exchange, for instance $l(r) = \mathrm{erf}(\omega r)$, which is much more problematic for functional parameterization, is treated by wave function theory (20). The ω parameter determines the length scale on which the short-range part decays and is typically approximately 0.8 Å^{-1}.
2. **Dispersion errors**. All the density functionals discussed above are semilocal in the correlation functional, meaning that they cannot capture long-range dispersion because that is a nonlocal density-density correlation (21). Yet dispersion interactions contribute significantly to supramolecular interactions such as those involved in a catalytic cycle. At a pragmatic level, progress has been made on this problem by the empirical addition of an atom-atom R^{-6} potential (22) that is damped at short range [typically called a -D correction

(23)]. More fundamentally, nonlocal van der Waals functionals are evolving toward useful accuracy and acceptable cost (24, 25). A third alternative is the addition of nonlocal correlation effects from the Kohn-Sham unoccupied orbitals via a second-order perturbation expression [typically called a double-hybrid functional (26)], although these currently carry too high a computational price for routine use on large systems at present.

3. **Strong correlation errors**. The Kohn-Sham reference wave function is a poor starting point for systems that exhibit strong correlations. Such systems have many other electron configurations whose importance is comparable to the Kohn-Sham configuration. As a consequence, the description of correlations in these systems through functionals of the electron density is very inadequate (27). Examples include metalloenzyme active sites such as the oxygen-evolving complex (28) where each of the four Mn atoms contains up to three spin-parallel d electrons, yet the overall spin state is a singlet. Addressing this challenge, however, takes us beyond both Kohn-Sham theory (29) and the scope of this review.

Density functionals that advance beyond the established local density approximation, GGA, and hybrid categories generally aim to address the self-interaction and/or dispersion errors listed above. One promising family of functionals is based on a range-separated version (30) of Becke's 1997 functionals (31) to reduce self-interaction (ωB97), or additionally with either a fraction of short-range exact exchange (ωB97X) or a dispersion correction (ωB97X-D) (32). These functionals are semiempirical in the sense that they contain 12–14 parameters that are fitted to approximately 400 precisely known energy differences. Importantly, they retain exactness for the UEG. Independent test data such as those shown in **Figure 1** establish transferability and illustrate the extent to which improvements can be obtained in chemical energy differences using these functionals relative to an established GGA (BLYP) and an established hybrid (B3LYP).

The basis sets used to generate the data in **Figure 1** are atomic orbital expansions. Functionals are developed at the complete basis set limit; therefore, reasonably large atomic orbital basis sets must be used to obtain calculated relative energies of the quality that the functional is capable of. For example, for light atoms such as C, N, O, and F, the basis set typically must contain

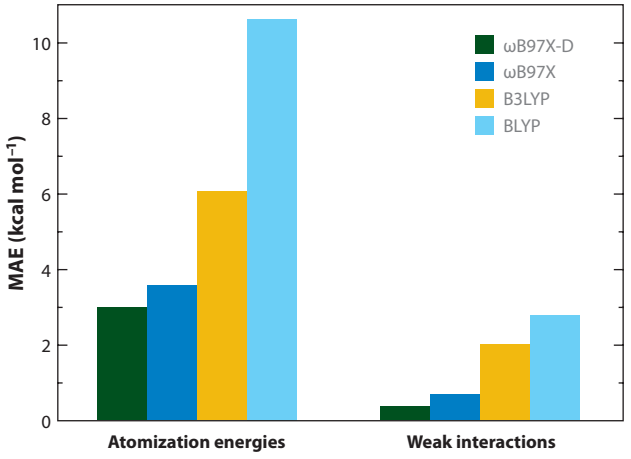

Figure 1

Independent comparison of an established generalized gradient approximation (BLYP) against an established hybrid (B3LYP), a range-separated hybrid (ωB97X), and a range-separated hybrid that includes an empirical long-range dispersion correction (ωB97X-D). The MAE (mean absolute errors) in atomization energies are for the 48 reactions comprising the G3/05 test set, and the MAE in weak interactions energies are for 25 intermolecular-complex binding energies. For details, see Reference 32.

approximately 30 functions, as typified by the triple-zeta basis sets that have 4s, 3p, 2d, and 1f shells of atomic orbitals. Smaller basis sets (for instance, 3s, 2p, and 1d function for the same light elements) can be used to explore potential energy surfaces, as described below, and then only for the final relative energies between stationary points evaluated with the larger basis sets. For more information on practical DFT calculations, the reader should consult additional references (33).

Returning to the question of functional selection, results of similar quality to the range-separated hybrids can be obtained with other recently developed functionals. One particular example is the family of hybrid meta GGA M06 functionals [meta indicates their inclusion of terms that are functionals of the kinetic energy density (34)], which comprises the M06, M06-2X, M06-L, and M06-HF functionals (35). The fact that carefully developed, range-separated hybrid functionals and hybrid meta GGAs can provide statistically significant improvements over established hybrids such as B3LYP is encouraging (36). At the same time, given that each family contains multiple members with differing strengths and weaknesses, these functionals have yet to attain the goal of universal applicability. Further improvements in the quality of density functionals of manageable complexity will almost certainly be obtained in the near future. Indeed, this is a very active area of research.

EXPLORING POTENTIAL ENERGY SURFACES

Reliable quantum mechanical electronic structure models provide an implicit description of the potential energy surface on which chemical transformations take place. They must be combined with reliable methods for the exploration of those surfaces (37, 38), with the final goal of producing reaction pathways for complex multistep catalytic processes, of the type illustrated in the following sections on applications. The reaction mechanism, including the relative energies of all minima and the potential energy barriers (transition structures) interconnecting them, in turn, is the basis for predicting overall kinetics. Two contradictory types of efficiency are desired. First, one wants to minimize the computer time required to identify the reaction mechanism. For this purpose, local search methods are well developed (37) and are briefly reviewed below—they are designed to converge to the nearest stationary point relative to the user-supplied guess. Second, one wants to minimize the human time required to identify the complete reaction pathway. For this purpose, one needs methods that interconnect the presumably known reactants and products (i.e., nonlocal path-finding methods). This active area of development (38) is discussed in more detail below. The number of energy and gradient evaluations required is one to two orders of magnitude greater than that needed for a local search.

Local Optimization Methods for Minima and Transition Structures

The computational cost of evaluating the analytical gradient of the DFT energy with any of the functionals discussed above is a relatively small multiple of the cost of an energy evaluation—typically approximately twice. Therefore, all searches for stationary points use gradients on every step. However, the cost of evaluating the analytical (or numerical) second derivative scales one power of system size greater than the energy or gradient. As a result, their use must be minimized because, for large enough systems, it completely dominates the cost of energy and gradient evaluation. Fortunately, the second derivatives are seldom necessary for local optimizations to structures that are minima. There are well-developed methods for identifying coordinate systems [typically either redundant (39) or nonredundant internal coordinates (40)] in which the optimization can proceed efficiently starting from a diagonal guess at the second-derivative matrix (though coordinate transformations become expensive for systems on the order of thousands of atoms).

Further knowledge about the second-derivative matrix is built up as the optimization proceeds, for instance, by quasi-Newton update methods (37).

By contrast, the most efficient local methods for transition-structure (saddle point) searches require the initial guess to be close enough to the answer that the second-derivative matrix exhibits the correct structure: one negative eigenvalue and the remainder positive. This is demanding for the user and means that more skill and experience are required to successfully execute transition structure searches. Furthermore, as one is walking uphill in one direction and downhill in the remaining ones (41), an exact calculation of the second derivatives at the point of the initial guess is typically needed to launch the calculation successfully, though some gradient-only algorithms are available (42).

Path-Finding Methods That Connect Different Minima

The motivation for automated path-finding methods can be clearly seen from the practical challenge of performing local optimizations for transition structures, relative to the comparatively routine task of local optimizations to minima. To discuss fully the development and current status of these techniques requires a separate review (38), so we confine ourselves to a short survey of basic methods followed by a slightly more detailed discussion of one modern approach, i.e., the growing-string method (GSM) (43, 44), which is used in the applications discussed subsequently.

Whereas stationary points on the potential energy surface are defined uniquely and are thus independent of working details such as the choice of coordinates, the paths that interconnect them are not. For example, the steepest descent path, $\mathbf{x}(s)$, going downhill from a given transition structure to a minimum, implicitly defined by $d\mathbf{x}/ds = -\nabla_{\mathbf{x}}E/|\nabla_{\mathbf{x}}E|$ is different in Cartesian coordinates versus mass-weighted coordinates versus any choice of internal coordinates. Perhaps the most important of these is the path in mass-weighted Cartesians, which corresponds to a zero-velocity classical trajectory (i.e., with infinite friction), which is also known as the intrinsic reaction coordinate (45). Additionally, there are, in general, multiple paths that interconnect two given minima, and one must identify the path that is most favored (as defined by the lowest free-energy barrier).

Given knowledge of reactant and product geometries, a crude linear interpolation between them is the most basic starting point for an optimization of the path connecting them. Points equally spaced along the path can be optimized to zero the gradient perpendicular to the linear path, so that the forces orthogonal to the initially guessed path are reduced to zero. This "drag and optimize" approach is effective only if the true path is close to linear. Otherwise, one is likely to be left with two "ends" of a path and a wide gap between them that includes the transition structure region. More-refined methods either begin with a better guess at the reaction path than that produced from linear interpolation (sometimes this may be chemically evident), or iterate the path from the crude initial guess with a chosen number of discretization points. Examples of methods in the latter category include the nudged elastic-band method (46), the string method (43), and the GSM (44). These methods are much more powerful in that the points on the calculated path (in principle) converge to the points on the true steepest descent path in the chosen coordinate system.

The GSM operates first in a growth phase in which discretization points are added to two strings (or subpaths) that begin from reactant and product, respectively. The overall vector of forces on the points in each substring is used to define a descent direction for refinement, after projection against the tangent at each contributing point (including a cubic spline interpolation joining the two substrings). The updated coordinates are then redistributed to have equal separation, and the process is repeated. When this force vector is considered small enough, a new point is added to

each substring, and this iterative growth process is continued until the substrings join. Subsequent refinement continues on the complete string until, after some hundreds or thousands of gradients, an acceptable approximation to the full steepest descent path is obtained. Although the number of gradients required is very large relative to typical local optimizations, no second derivative calculations are required, and the problem of guessing a suitable transition structure is removed. Several useful efficiency improvements have been described (47). Finally, a local optimization starting from the path point of highest energy is used to refine the transition structure (48). Although the GSM is a useful tool that has been used in a growing range of applications in catalysis and elsewhere, there is considerable ongoing work to improve the efficiency of path-finding methods, for instance, by incorporating as much of the refined technology associated with local search methods as possible.

ILLUSTRATIONS OF THE APPLICATION OF QUANTUM CHEMICAL CALCULATIONS TO PROBLEMS IN CATALYSIS

The application of quantum chemical calculations to the field of catalysis is illustrated through four examples drawn from the authors' work. The first two deal with issues pertaining to homogeneous catalysis, and the second two deal with issues pertaining to heterogeneous catalysis. These illustrations show the variety of chemical insights that can be gained from electronic structure calculations and the extent to which predicted rate parameters agree with experimental observations.

Solvent Effects on the Dissociation of Iron^{III}[Tetrakis(Pentafluorophenyl)]Porphyrin Chloride

Iron^{III}[tetrakis(pentafluorophenyl)]porphyrin chloride, here abbreviated as PFeCl (**Figure 2**), is catalytically inactive for cyclooctene epoxidation by hydrogen peroxide or hydrogen peroxide decomposition when dissolved in acetonitrile but is active if the solvent contains methanol (MeOH) (49, 50). The shift in the ^{1}H NMR signal of the β-pyrrole protons on the porphyrin ring observed when solvent contains methanol suggests that methanol facilitates the dissociation of PFeCl into PFe^+ and Cl^- and that methanol coordinates axially to the Fe^{III} center to form $PFe(MeOH)^+$. The rate of cyclooctene epoxidation by hydrogen peroxide is then observed to be linear in the concentration of $PFe(MeOH)^+$, and the concentration of this species is determined from the

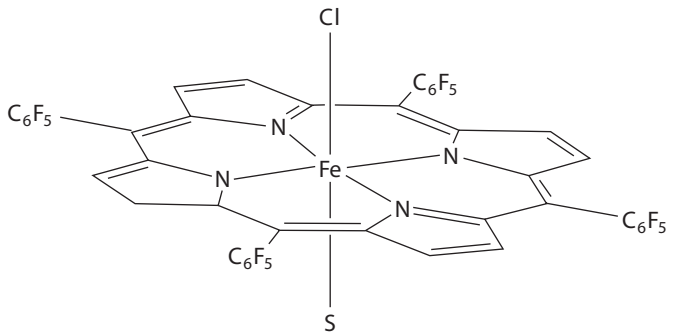

Figure 2

Iron^{III} [tetrakis-(pentafluorophenyl)]-porphyrin systems with two axial ligands: S = MeOH and MeCN.

equilibrium constant for the following reaction:

$$PFeCl_{sol} + MeOH_{sol} \leftrightharpoons PFe(HOMe)^{+}{}_{sol} + Cl^{-}{}_{sol.} \quad 1.$$

The difference in the change in Gibbs free energy for Reaction 1 occurring in pure methanol versus pure acetonitrile, $\Delta\Delta G^0$, was estimated experimentally to be -20.7 ± 1.0 kJ mol^{-1}. However, the extent to which methanol enhances the dissociation of the porphyrin salt as a consequence of coordination to PFe^+ as opposed to its solvation of $PFe(MeOH)^+$ and Cl^- could not be determined by experimental observation. This question has been addressed through theoretical analysis of solute-solvent interactions (51).

Solvent-solute interactions were described using a discrete/continuum, or quasi-chemical, model (52–55). The first shell of solvent molecules was represented explicitly, taking into account only the most stable configuration of the cluster, and the remaining solvent was described as a continuum dielectric. The solvation free energy (the excess chemical potential) of solute X was expressed in terms of the solvation free energy of the cluster, $\Delta G^0_{ex,S}(S-X)$, and the gas-phase free energy of cluster formation, $\Delta G^0_{ig,form}(S_n - X)$:

$$\Delta G^0_{ex,S} = \Delta G^0_{ig,form}(S_n - X) + \Delta G^0_{ex,S}(S_n - X) - n\Delta G^0_{ex,S}(S-X) - nRT\ \ln[S]. \quad 3.$$

The first three terms of Equation 3 represent the free energies of three elementary steps in which a gas-phase solute particle (molecule or ion) is placed into the solvent. In the first step, n solvent molecules S are removed from the solvent to the gas phase (term 3), then n solvent molecules interact with the solute in the gas phase to form cluster $S_n - X$ (term 1). Finally, the cluster is placed into the solvent (term 2). The fourth term in Equation 3 is a correction for the solvent concentration. The geometries of the solvated porphyrins systems were carried at the DFT/EDF1/6-31G level, whereas calculations for the chloride anion and methanol were done at the MP2/6-31G(+,+)G(d,p) level. Nonspecific solvation energies were calculated with the surface and simulation of volume polarization for electrostatics continuum [SS(V)PE] model (56).

The value of $\Delta\Delta G^0$ was then evaluated as

$$\Delta\Delta G^0 = \Delta\Delta G^0_{ex}(Cl^-) + \Delta\Delta G^0_{ex}(PFe(HOMe)^+) - \Delta\Delta G^0_{ex}(MeOH) - \Delta\Delta G^0_{ex}(PFeCl). \quad 4.$$

Each term in Equation 4 was determined by taking the differences in the values of $\Delta G^0_{ex,S}$ for each solute species dissolved in pure methanol or acetonitrile using Equation 3. This led to the following results:

$$\Delta\Delta G^0_{ex}(MeOH) \approx -10\ kJmol^{-1}$$
$$\Delta\Delta G^0_{ex}(PFeCl) \approx -6\ kJmol^{-1}$$
$$\Delta\Delta G^0_{ex}(PFe(HOMe)^+) \approx -9\ kJmol^{-1}$$
$$\Delta\Delta G^0_{ex}(Cl^-) \approx -30\ kJmol^{-1}.$$

Thus, the final estimate for the difference in the dissociation free energies in methanol and acetonitrile is $\Delta\Delta G^0 \approx -23$ kJmol^{-1}, in very good agreement with the experimental value of -21 kJ mol^{-1}.

This example shows that, despite the simplicity of the quasi-chemical model, the origin of the strong solvent effect on the dissociation of PFeCl can be understood. Dissociation of PFeCl is energetically more favorable in methanol than in acetonitrile primarily because of the strong specific interactions between the chloride anion and solvent methanol molecules in its first solvation shell. These interactions are weaker in acetonitrile. Energy decomposition analysis of chloride-solvent interactions suggests that superior solvation of Cl^- anions in methanol is due to a higher contribution of charge delocalization for Cl^--MeOH than for Cl^--MeCN interactions. The

differences in the solvation energies of the other species participating in the dissociation process are also noticeable but contribute to the observed solvent effect to a lesser extent.

Effects of Ligand Composition on the Oxidative Carbonylation of Toluene to Toluic Acid Catalyzed by Rh^{III} Complexes

The oxidative carbonylation of aromatic hydrocarbons to produce carboxylic acids can be catalyzed by Rh^{III} cations in the presence of moderately strong acids such as trifluoroacetic acid, whereas weak acids, such as acetic acid, are ineffective. It has been suggested that the effect of acid composition on the oxidative carbonylation of arenes is due to the influence of anionic ligands on the electrophilicity of Rh^{III} (57, 58). Implicit in this interpretation is the assumption that the rate-limiting step in oxidative carbonylation of aromatic compounds is electrophilic activation of a C-H bond on the aromatic ring. What is not addressed, though, is the extent to which ligand composition affects the strength of arene coordination and the activation energy for activation of the C-H bond. To address these issues, we have carried out a theoretical analysis of the oxidative carbonylation of toluene by Rh^{III} complexes and have investigated the effects of ligand composition on toluene coordination and activation of the C-H bonds on the arene ring (59).

Experimental and theoretical investigations of the mechanism and kinetics of the oxidative carbonylation of toluene to toluic acid carried out in the presence trifluoroacetic acid (TFAH) suggest that when the solvent is the reactant itself, Rh^{III} is stable as a cation-anion pair (57, 60–62). Our theoretical work further suggests that the species responsible for the activation of toluene is $Rh(CO)_2(TFA)_3$. In the course of the reaction, Rh^{III} is reduced to Rh^{I}, which must then be reoxidized to close the catalytic cycle. If NH_4VO_3 is used as the oxidant, the rate of reoxidation is much more rapid than the rate of reduction; hence, Rh is present predominantly as Rh^{III} (13). Combined spectroscopic and theoretical work confirms that the resting state of the catalyst is $Rh(CO)_2(TFA)_3$ (63).

Figure 3 illustrates the mechanism for the oxidative carbonylation of toluene to toluic acid catalyzed by $Rh(CO)_2(TFA)_3$ when $[VO_2]^+$ cations serve as the oxidizing agent for the reoxidation of Rh^{I} to Rh^{III} (62, 63). Both experimental and theoretical studies suggest that the first step in the oxidative carbonylation of toluene is the coordination of toluene by Rh^{III} followed by C-H bond activation of the arene to produce an Rh-arene complex and TFAH. Theoretical analysis of the process shows that the coordination of toluene to the Rh complex is equilibrated and that C-H bond activation is the rate-limiting step (62, 63).

Electronic structures and energies of reactants, products, and transition states were determined at the DFT/ B3LYP/6-31G* level, whereas the LANL2DZ effective core potential was used for Rh. The energy for each optimized geometry was then updated using the 6-311G**/LANL2DZ basis set. The GSM was used to locate the transition state connecting two minimum energy structures (44). Vibrational analysis was performed to ensure the nature of energy minima and transition states as well as to generate thermochemical data.

The kinetics for the oxidative carbonylation of toluene can be represented by Reactions 2 and 3, illustrated for the case in which TFA anions serve as the ligands:

$$Rh(CO)_2(TFA)_3 + C_7H_8 \rightleftharpoons Rh(CO)_2(TFA)_3(C_6H_5CH_3) \quad 2.$$

$$Rh(CO)_2(TFA)_3(C_6H_5CH_3) \rightarrow Rh(CO)_2(TFA)_2(TFAH)(C_6H_4CH_3). \quad 3.$$

The rate of toluene activation, r, can then be written as

$$r = k_{app}[Rh][CH_3C_6H_5], \quad 5.$$

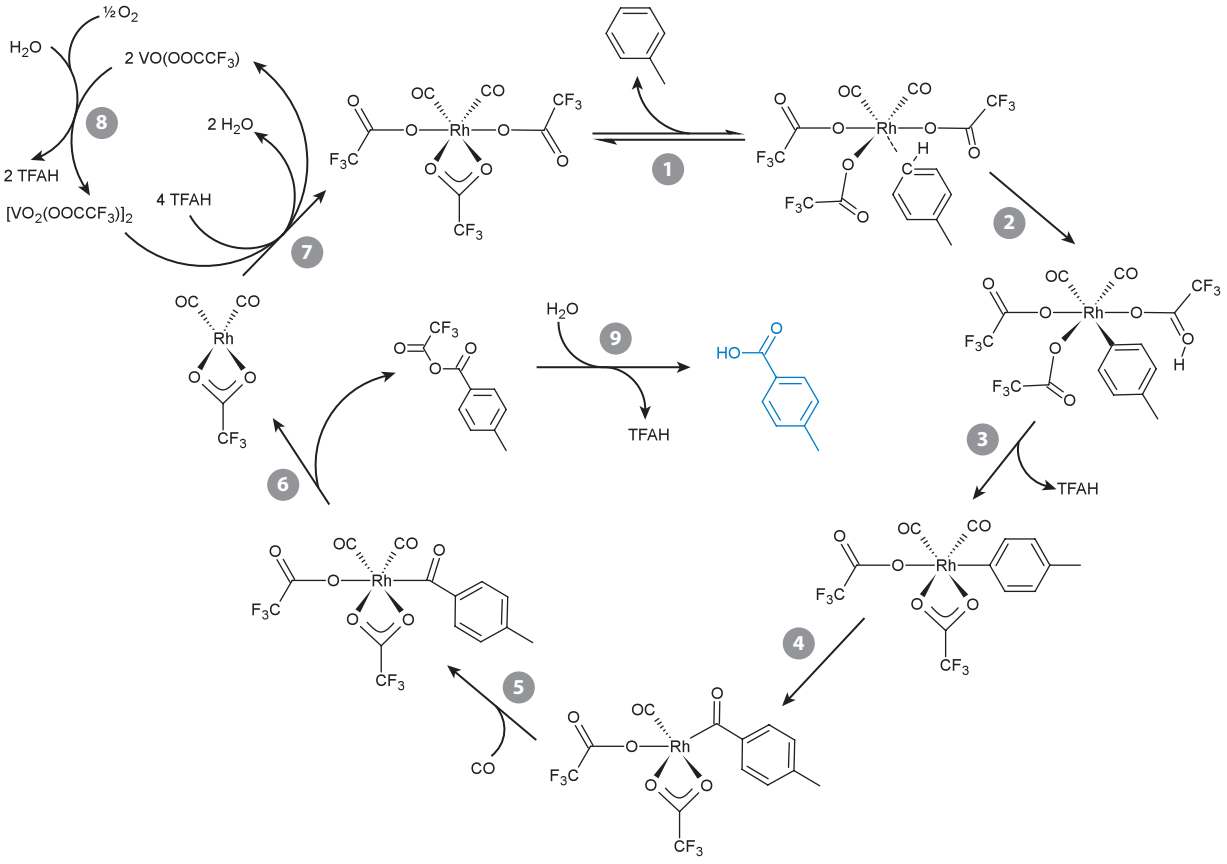

Figure 3

Proposed mechanism for the oxidative carbonylation of toluene to toluic acid catalyzed by Rh^{III} in the presence of trifluoroacetic acid. VO_2^+ serves as the oxidizing agent for the reoxidation of Rh^I to Rh^{III} (59).

where

$$k_{app} = K_{coord} k_{act}. \qquad 6.$$

In Equations 5 and 6, k_{app} is the apparent rate coefficient for the oxidative carbonylation of toluene, k_{act} is the intrinsic rate coefficient for activation of the C–H bond, K_{coord} is the equilibrium constant for the coordination of toluene to the complex $Rh(CO)_2(TFA)_3$, and [Rh] and $[CH_3C_6H_5]$ are the concentrations of $Rh(CO)_2(TFA)_3$ and toluene, respectively. The turnover number (TON) based on the formation of toluic acid can then be expressed as follows, assuming that the reaction occurs in a well-stirred batch reactor:

$$\mathrm{TON} = \frac{[CH_3C_6H_4COOH]}{[Rh]_0} = \frac{[CH_3C_6H_5]_0}{[Rh]_0}(1 - \exp(-k_{app}[Rh]_0 t)). \qquad 7.$$

In this expression, $[Rh]_0$ and $[CH_3C_6H_5]_0$ represent the concentrations of Rh and toluene loaded into the reactor.

Figure 4*a* shows the number of turnovers predicted from Equation 4 after 4 h of reaction. The highest TON occurs for $CClF_2COOH$, and the value of the TON for this acid is ~500. Both findings are in good agreement with those observed experimentally (see **Figure 4*b***). However,

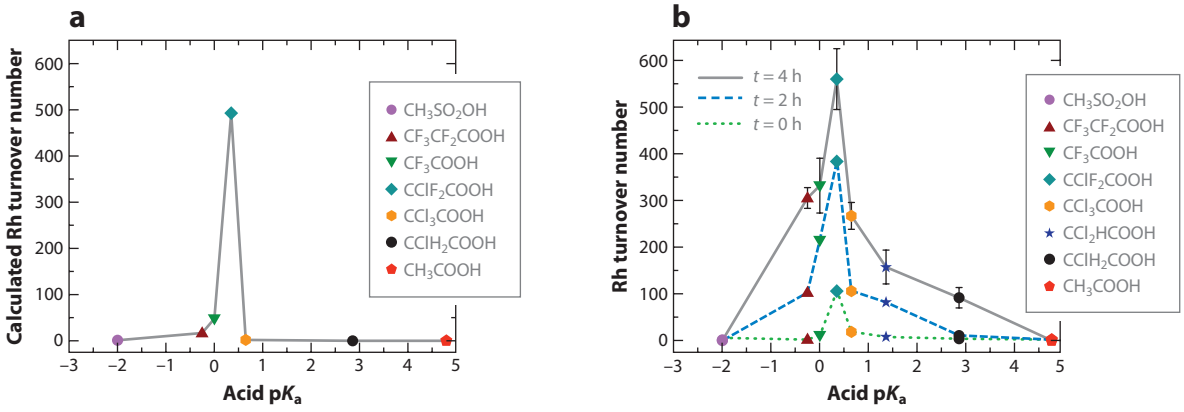

Figure 4

(*a*) Turnover numbers calculated from Equation 4 using apparent rate coefficients determined theoretically and (*b*) turnover numbers for Rh-catalyzed oxidative carbonylation of toluene to toluic acid versus pK_a of designated acid. Reaction conditions: 37.5 mmol toluene (3.46 g); 13.0 mmol designated acid; 3.8 mmol corresponding anhydride; 10 μmol Rh(acac)3 (0.0039g), 0.5163 mmol NH4VO3 (0.0604 g); $P_{CO} = 0.345$ MPa; $P_{O2} = 0.345$ MPa; $T = 353$ K (59).

the decrease in TON for acids with higher or lower pK_a than that of $CClF_2COOH$ (p$K_a = 0.35$) is more rapid than the values noted in **Figure 4*b***. The variation in the TON with the pK_a of the acid from which the anionic ligand is derived can be interpreted in terms of the value of ΔG_{app}, defined as $\Delta G_{app} = \Delta G^0_{coord} + \Delta G^{\ddagger}_{act}$, because k_{app} is exponentially dependent on ΔG_{app} (see **Figure 5**). The lowest value of ΔG_{app} is for $CClF_2COOH$. Accordingly, the value of k_{app} and the TON determined from Equation 4 (see **Figure 4*a***) are the largest. The sharpness of the change in the TON with acid pK_a is attributable to the change with acid composition in the value of $\Delta\Delta G_{app}$, the difference in the apparent Gibbs free energy of activation relative to that calculated for $CClF_2COOH$. For example, the values of $\Delta\Delta G_{app}$ are 3.9 kcal mol^{-1} for CCl_3COOH and 1.7 kcal mol^{-1} for CF_3COOH compared with $CClF_2COOH$. **Figure 4b** suggests that $\Delta\Delta G_{app}$ should be $\sim \pm 1$ kJ mol^{-1} to obtain the experimentally observed results. Thus, although the values of ΔG_{app} determined theoretically reproduce the trends seen experimentally, the differences in

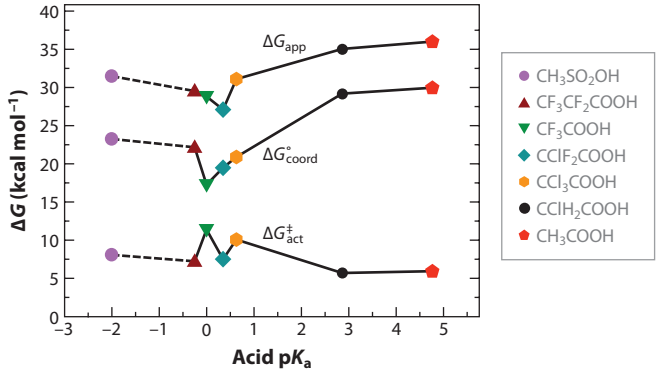

Figure 5

Gibbs free energy of toluene coordination and C–H bond activation and apparent Gibbs free energy of activation as a function of the pK_a of the acid from which the anionic ligand was derived (59).

the value of this quantity are not calculated accurately enough to capture the magnitude of the observed changes in the TONs. Solvent interactions with the catalyst may also contribute to charge delocalization, which could result in the gradual decrease observed experimentally.

To summarize, the minimum in the ΔG_{app} with pK_a, shown in **Figure 4**, is a consequence of the combined effects of anionic ligand composition on the apparent energy and entropy of activation. The changes in each of these effects with ligand composition are subtle and can be appreciated only through careful theoretical analysis.

Selective Oxidation of Methanol to Formaldehyde on Silica-Supported Monovanadate Species

Isolated (mono)vanadate species supported on silica are active for the selective oxidation of methanol to formaldehyde (64–72). Experimental characterization using XANES, EXAFS, and Raman spectroscopy shows that monovanadate species have a distorted tetrahedral geometry containing three V-O support bonds and one V=O vanadyl bond (66, 73). The intrinsic kinetics of methanol oxidation to formaldehyde measured at low methanol conversion are first order in methanol and zero order in oxygen, suggesting that the majority of the V atoms in the catalyst are present as V^{5+} under reaction conditions, a conclusion supported by in situ Raman observations (66). Experimental studies suggest that the adsorption of methanol to form V-OCH_3 species is reversible and that the rate-limiting step in the formation of formaldehyde is the transfer of a hydrogen atom from this species to an oxygen atom associated with the catalyst (65, 67, 71), possibly to the V=O bond of the active center (66).

The mechanism of methanol oxidation on silica-supported monovanadate species has been investigated theoretically (74–76). Although different models of the silica support were used in each study, the calculated heats of methanol adsorption and the activation energy for the rate-limiting step were very similar and agree well with experimental values. However, neither of these studies was able to reproduce experimentally the observed turnover frequencies, owing largely to errors in the magnitude of the predicted pre-exponential factors for the adsorption equilibrium constant and the rate coefficient for the rate-limiting step. Likewise, the mechanism by which vanadium centers are reoxidized following methanol oxidation and the rate at which this process occurs were not examined. Both of these issues have recently been addressed through a theoretical analysis of the complete catalytic cycle (76).

Alternative models for the surface of amorphous silica were examined in an effort to find a representation consistent with experimental observations and yet tractable from the standpoint of computational costs. Clusters isolated from the low-index surfaces of β-crystoballite as well as silsesquioxane ($Si_8O_{12}H_8$) were examined. The model based on silsesquioxane was best for capturing the physical properties of silica with a reasonable expenditure of computational effort. VO_x/SiO_2 was modeled by replacing one of the eight Si-H groups in the silsesquioxane cube by a vanadyl group, V=O. The resulting silica-supported VO_4 species has a distorted tetrahedral geometry containing three V-O-Si support bonds and one V=O vanadyl bond (see **Figure 6**).

Geometry optimization with full relaxation of all atoms was performed at the DFT/ B3LYP/6-31G* level. After structural optimization, a more accurate estimate of the energy was calculated using the LACV3P**++ basis set (77). The electronic structure of vanadium was described using the LANL2DZ basis set. Calculated frequencies were scaled by 0.9614 to account for the overestimation of vibrational frequencies determined at the B3LYP/6-31G* level of theory (78). The GSM (44) was used to find an initial estimate for transition-state geometries, also using the B3LYP/6-31G* level of theory. Estimated transition-state geometries were then refined using the Berny optimization algorithm (79, 80). The final value of the transition-state energy was calculated

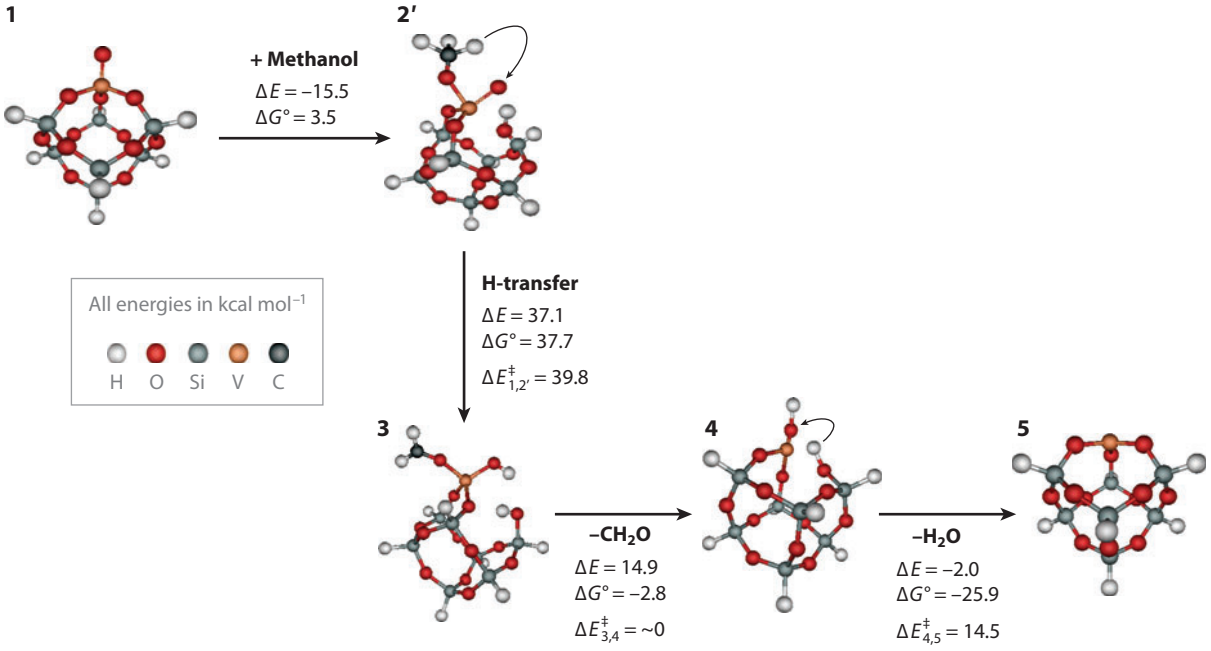

Figure 6

Selective oxidation of methanol to formaldehyde over vanadate species 1. Vanadium is reduced to V^{3+} in species 5. ΔE and ΔG^0 are shown in kcal mol^{-1} at 650 K (77).

using the LACV3P**++ basis set for all atoms except V, which was described using the LANL2DZ basis set. The broken-symmetry approach (81) was used to calculate the energy of the transition state for reactions involving multiple spin states, which have a biradicaloid electronic structure. The thermally averaged spin-transition probabilities for nonadiabiatic crossing from the singlet to the triplet potential-energy surface were determined using the Landau-Zener equation (83). This analysis showed that the rate of spin-surface crossing is much faster than the rate-limiting H-abstraction step and, hence, that activation energies determined on the triplet-state surface could be used for the necessary rate calculations. The Gibbs free energy for each ground- or transition-state structure was calculated using standard relationships from statistical mechanics (84–87). All parameters were evaluated at 650 K, the temperature at which the selective oxidation of methanol to formaldehyde was studied experimentally.

The mechanism of methanol oxidation to formaldehyde is illustrated in **Figure 6**. Methanol adsorption is followed by the transfer of a hydrogen atom from the methoxide group of 2′ to the vanadyl group of this species to form a vanadium hydroxyl group 3. The formaldehyde molecule associated with group 3 can readily desorb, as the change in Gibbs free energy for this process is $\Delta G^0 = -2.8$ kcal mol^{-1}, a result that is in agreement with experimental observation (89). The remaining two hydroxyl groups associated with species 4 react to form water and reform a support V–O–Si bond (the reaction of form 4 to form 5). The vanadium in species 5, formed upon desorption of water, must be reoxidized to complete the catalytic cycle. Experimental studies suggest that this process is very rapid and, hence, kinetically irrelevant as evidenced by a zero-order dependency of the rate of formaldehyde formation on oxygen partial pressure (66, 71, 72). Consistent with this conclusion, in situ Raman spectroscopy shows that virtually all of the vanadium remains in the +5 state under reaction conditions (67). Theoretical analysis of the reoxidation

process confirms that the rate of this process is four orders of magnitude faster than the rate at which vanadium centers are reduced from +5 to +3 (77).

Analysis of the Gibbs free-energy changes associated with the elementary steps for methanol oxidation occurring on silica-supported monovanadate species indicates that methanol adsorption is quasi-equilibrated and that the rate-limiting process at low methanol conversions is the process leading from species 2′ to 3 (see **Figure 6**). The rate of formaldehyde formation, R_{CH_2O}, and the apparent rate constant, k_{app}, are respectively given by

$$R_{CH_2O} = k_{app} P_{MeOH} \quad 8.$$

and

$$k_{app} = K_{1,2'} k_{2',3} = k^0_{app} \exp\left(\frac{-\Delta E_{app}}{RT}\right), \quad 9.$$

where $K_{1,2'}$ is the equilibrium constant for the adsorption of methanol as 2′, $k_{2',3}$ is the rate constant for the rate-limiting step, ΔE_{app} is the apparent activation energy, and P_{MeOH} is the partial pressure of methanol. The equilibrium constant for methanol adsorption can be evaluated using Equation 10.

$$K_{1,2'} = \sigma_{1,2'} \frac{q_{2'}}{q_{MeOH} q_1} \exp\left(\frac{PV}{RT}\right) \exp\left(\frac{-\Delta E_{1,2'}}{RT}\right), \quad 10.$$

where q_i is the partition function for species i and $\sigma_{1,2'}$ is the symmetry factor for the reaction of 1 to 2′. Because any one of the three V–O–Si support bonds can be broken, $\sigma_{1,2'}$ is equal to 3. The rate constant, $k_{2',3}$, was determined from the following expression:

$$k_{2',3} = \sigma_{2'3} \kappa(T) \frac{k_B T}{h} \frac{q^{\ddagger}_{2',3}}{q_{2'}} \exp\left(\frac{-\Delta E^{\ddagger}_{2',3}}{RT}\right). \quad 11.$$

In Equation 11, $q^{\ddagger}_{2',3}$ and $q_{2'}$ are the partition function for the transition state involved in the transformation of species 2′ to 3 and the partition function for species 2′, respectively. The symmetry factor, $\sigma_{2',3}$, in the pre-exponential factor is equal to 3 because any one of the three hydrogen atoms in the methoxy group of species 2′ can transfer to the vanadyl group. The transmission coefficient, κ, for tunneling is included because the transition state involves transferring a hydrogen atom. Wigner's approximation to the barrier, which uses an Eckart potential, was applied in calculating κ (90).

A comparison of our computed values for $K_{1,2'}$, $k_{2',3}$, and k_{app} at 650 K with those obtained in previous theoretical (75) and experimental studies (66, 71, 72) are presented in **Table 1**. The value of $\Delta E_{1,2'}$ for the adsorption of methanol as species 2′ is lower than that determined by Sauer and coworkers (75) by 6.0 kcal mol^{-1} but only 2.1 kcal mol^{-1} lower than that determined from the experimental observations of Wachs and coworkers (71, 72). The difference in the two theoretical values of $\Delta E_{1,2'}$ is likely a consequence of the basis sets used. As noted above, the absolute value of $K_{1,2'}$ determined at 650 K is in reasonable agreement with that determined from the results of the latter researchers. The activation energy associated for the rate-limiting step determined in the present study is 3.0 kcal mol^{-1} higher than that reported by Sauer and coworkers (75). By contrast, the apparent activation energy calculated in the present study is 3.0 kcal mol^{-1} lower than that predicted by Sauer and coworkers (75) but only 1.3 kcal mol^{-1} higher than that reported in the experimental work of Bronkema & Bell (66). More notably, the preexponential factor for the apparent first-order rate coefficient, k^0_{app}, determined in the present study agrees closely with that found experimentally but is an order of magnitude larger than that determined from the results reported by Sauer and coworkers (75). As shown in **Table 1**, the value of k_{app} evaluated at 650 K is within a factor of two of that measured experimentally. By contrast, the value of k_{app}

Table 1 Comparison between theoretical estimates and experimental measurements of the rate parameters for methanol oxidation to formaldehyde (77)

		Theory	Theory[a]	Experiment
Adsorption step	$\Delta E_{1,2'}$ (kcal mol^{-1})	−15.5	−9.5	−13.4[b], −13.3[c]
	$K_{1,2'}{}^{o}$ (atm^{-1})	2.60×10^{-5}	–	5.12×10^{-5}[b], 2.04×10^{-4}[c]
	$K_{1,2'}$ (atm^{-1})	4.23	–	1.64[b,d], 6.04[c]
Rate-limiting step	$\Delta E^{\ddagger}_{2',3}$ (kcal mol^{-1})	39.8	36.8	–
	$k_{2',3}{}^{o}$ (s^{-1})	1.92×10^{12}	–	–
	$k_{2',3}$ (s^{-1})	0.0795	–	–
Apparent kinetics	ΔE_{app} (kcal mol^{-1})	24.3	27.3	23 ± 1[c]
	$k_{app}{}^{o}$ (atm^{-1} s^{-1})	4.00×10^{7}	1.34×10^{6}	1.90×10^{7}[c]
	k_{app} (atm^{-1} s^{-1})	0.27	8.86×10^{-4}	0.35[c]

[a]Reference 75.
[b]Reference 70.
[c]Reference 66.
[d]Reference 71.

determined from the work of Sauer et al. (74) is three orders of magnitude smaller than that observed experimentally.

This illustration demonstrates the extent to which the rate parameters for reactions occurring at well-defined catalytic centers can be described using a combination of quantum theory and absolute-rate theory. Requirements for such analysis include the following: The experimental studies must provide a sound basis for describing the composition and structure of the active site, experimental information must be available to identify the reaction pathway, and the electronic structure calculation must be carried out at an adequately high level.

Benzene Alkylation with Ethene over H-ZSM-5

Ethylbenzene is an intermediate in the production of styrene (91), a paint solvent, and an intermediate in the pharmaceutical industry (92). ZSM-5, a medium-pore zeolite, is particularly well suited for the gas-phase alkylation of aromatics (93–95). Mechanistic studies of benzene ethylation catalyzed by H-ZSM-5 conclude that this process is best described by a Langmuir-Hinshelwood mechanism, in which the initial step is the coadsorption of the reactants at the acid site (96, 97).

Several theoretical studies of benzene ethylation over zeolites have been reported (98–101). In these investigations, the Brønsted-acid site and a portion of the zeolite framework surrounding the active site were represented by a cluster containing 4 to 84 T atoms. Heats of adsorption and activation energies were then carried out at the DFT/B3LYP level, using a spectrum of basis sets. To illustrate this approach and its limitations, we summarize the findings of our own recent study of benzene ethylation on H-ZSM-5 (102). Both a one-step scheme, in which the precursor is represented by coadsorbed ethene and benzene at the acid site, and a two-step mechanism, in which ethene is first protonated to form an ethoxide species that subsequently reacts with benzene to form the product, ethylbenzene, were considered. All calculations were done for the Al12-O20(H)-Si3 site (103). The rate coefficients for these elementary steps, together with diffusivities obtained from molecular dynamics simulations, were then used in a continuum model of a zeolite crystal to calculate the overall activity as a function of the gas-phase conditions (104). These studies revealed important shortcomings in the model used, because the theoretically determined rate coefficients for the one-step mechanism had to be increased by two orders of magnitude to achieve agreement

with experimental data (105) while the rate coefficients for the two-step mechanism had to be lowered by a factor of four. Moreover the apparent activation energy determined for the one-step mechanism was too low by 15 kJ mol^{-1}, whereas that for the two-step mechanism was slightly higher than the experimental values. These findings motivated a reexamination of the methods used to calculate the rate parameters for reactions occurring in zeolites.

Recent studies have shown that the accuracy of DFT for simulation of reactions occurring in zeolites is hampered by the use of functionals that are computationally efficient but do not properly account for long-range dispersion interactions (106, 107) and are subject to the self-interaction error (108, 109). This situation results in underestimation of adsorption energies (110) and energy barriers (112, 113). An approach for determining more accurate value energies in extended systems is to use a hybrid scheme, such as the MP2:DFT scheme introduced by Tuma & Sauer (110, 114). This approach combines MP2 calculations with Gaussian basis sets for the reaction site and plane-wave DFT for the full system under periodic boundary conditions. For a series of cluster models (**C**), a size-dependent high-level correction, defined as the difference between MP2 and DFT energies, is calculated.

We have used the MP2:DFT hybrid scheme to revise our previous DFT calculations for the alkylation of benzene with ethene over zeolite H-ZSM-5 (115). The final estimates of adsorption energies and energy barriers were calculated in three steps. First, a structure optimization for the entire H-ZSM-5 unit cell was carried out using DFT with periodic boundary conditions. Note that, in contrast to the original approach but following Reference 116, hybrid MP2:DFT structure optimizations were not performed because of (*a*) the computational expense of these calculations

Table 2 Adsorption energies using the hybrid DFT:MP2 scheme and the PBE+D adsorption energies at the PBE optimized structures (115)[a]

Species number (see Figure 7)	1	2	3	4	5	6	7[b]
$\Delta E(\mathbf{S})_{PBE}$	−31.5	−24.0	−16.6	−40.7	−53.5	−2.0	−4.2
$\Delta \tilde{E}(\mathbf{S})_{high}$	−26.7[c]	−76.2[d]	−118.3	−122.6	−27.5	−95.8	−20.5
$\Delta E(\mathbf{C}_{18})^{CBS}_{MP2}$	5.8	14.2	13.8	14.8[e]	12.9	11.7	7.7
$\Delta E(\mathbf{C}_3)_{CCSD(T)}$[f]	4.1	5.5	6.1	7.5	6.9	3.9	0.5
$\Delta \tilde{E}(\mathbf{S})_{final\ estimate}$	−48.3	−80.5	−115.1	−141.0	−61.3	−82.2	−16.5
Difference to PBE	−16.8	−56.5	−98.5	−100.3	−7.7	−80.2	−12.3
$\Delta E(\mathbf{S})_{ZPV}$	1.4	−0.2	2.8	6.4	10.5	4.1	−1.9
$\Delta H(\mathbf{S})_{298} - \Delta E_0(\mathbf{S})_{PBE}$[g]	1.1	2.6	2.3	3.9	−2.6	3.0	4.7
$\Delta H(\mathbf{S})_{653} - \Delta E_0(\mathbf{S})_{PBE}$[h]	6.5	8.5	7.2	14.2	0.3	8.5	11.6
$\Delta E(\mathbf{S})_{D//PBE}$	−29.2	−63.0[i]	−100.8	−97.7	−33.7	−73.6	−18.8
$\Delta E(\mathbf{S})_{PBE+D//PBE}$	−60.6	−86.9	−117.4	−138.3	−87.3	−75.6	−23.0
$\Delta E(\mathbf{C}_{18})^{DFT+D}_{high}$	1.2	−11.4	−12.1	−10.9[e]	3.2	−11.7	−2.7
$\Delta E(\mathbf{S})^{DFT+D}_{final\ estimate}$	−49.5	−78.7	−109.6	−126.9	−64.3	−71.7	−17.5

[a]Energies as predicted with the parameters of Grimme (119). Zero-point vibrational energies and thermal contributions to adsorption enthalpies are also included. All energies are in kJ mol^{-1} (115).

[b]Adsorption in channel intersection.

[c]This value remains the same for Al-O-$Si(OH)_3$ instead of Al-O-H termination.

[d]−76.5 kJ mol^{-1} for the second set of unit cell parameters.

[e]For 16T cluster.

[f]Difference between CCSD(T) and RI-MP2 adsorption energies on a 3T cluster.

[g]Contribution to enthalpy at 298 K. $\Delta E_0(\mathbf{S})_{PBE}$ is the ZPVE corrected adsorption energy.

[h]Contribution to enthalpy at 653 K. $\Delta E_0(\mathbf{S})_{PBE}$ is the ZPVE corrected adsorption energy.

[i]−60.9 kJ mol^{-1} for the second set of unit cell parameters.

and (*b*) the small effect of high-level structure-relaxation effects. Second, single-point MP2 and DFT calculations were conducted on clusters of increasing size cut out from the plane-wave DFT optimized structures to determine the periodic MP2 limit by extrapolation. Third, single-point MP2 calculations with increasing basis set size were performed to determine the complete basis set limit. Additionally, CCSD(T) calculations on small cluster models were carried out, to account for higher-order correlation effects.

The final estimates of the hybrid MP2:DFT adsorption energies obtained from the sum of the PBE energy, the high-level correction extrapolated to the periodic limit, the complete basis set limit correction, and the CCSD(T) corrections are presented in **Table 2** for each of the processes listed in **Figure 7**. The differences between the final estimates and the PBE results are substantial. For the physisorption structures 1–4 and 6–7, they are between 6.2 and 13.4 kJ mol^{-1} per CH_n unit. For ethylbenzene (structure 3) and the coadsorption of ethene and benzene (structure 4), the total difference is as large as 100 kJ mol^{-1}. There are not only substantial quantitative changes, but also qualitative ones. PBE predicts the counterintuitive sequence ethene > benzene > ethylbenzene for the adsorption strength, whereas our final estimates reverse this sequence.

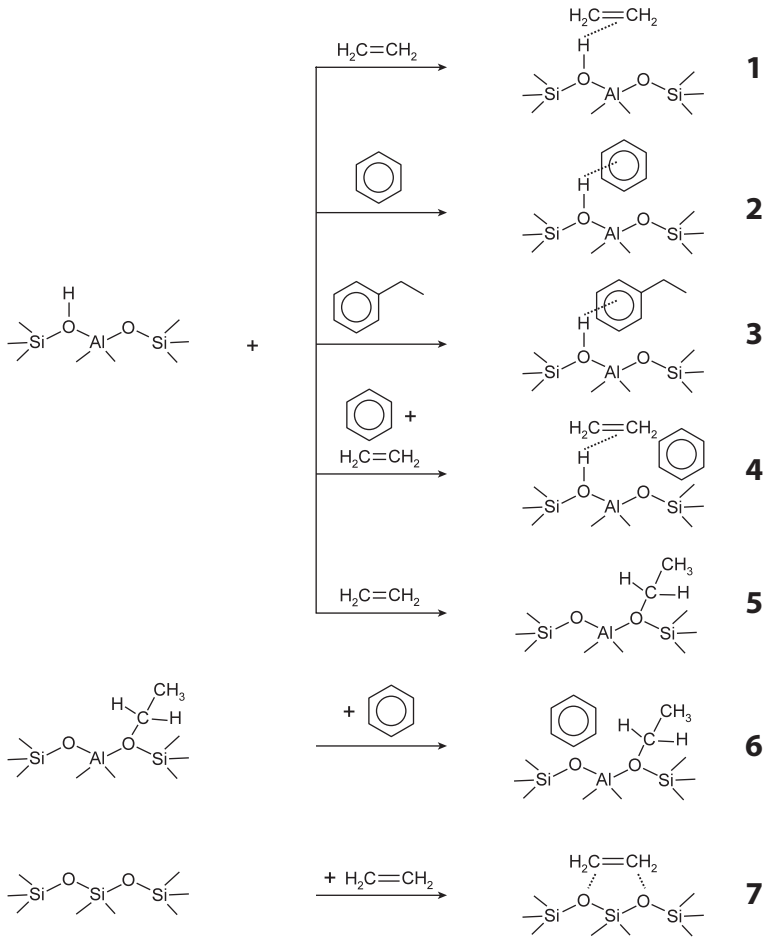

Figure 7

Elementary processes involved in the alkylation of benzene with ethene.

Table 3 Intrinsic energy barriers obtained using the hybrid MP2:DFT scheme and the PBE+D intrinsic energy barriers at the PBE optimized structures (115)[a]

Species number (see Figure 7)	1s	1s, rev	2s(1)	2s(1), rev	2s(2)	2s(2), rev
$E^{\ddagger}(\mathbf{S})_{\mathrm{PBE}}$	84.3	173.1	91.6	113.7	95.9	169.9
$\Delta\tilde{E}^{\ddagger}(\mathbf{S})_{\mathrm{high}}$	43.9	58.1	39.3	40.2	7.4	21.1
$\Delta E^{\ddagger}(\mathbf{C}_{16})^{\mathrm{CBS}}_{\mathrm{MP2}}$	1.0	2.5	0.6[b]	−6.5[b]	0.2	10.4
$\Delta E^{\ddagger}(\mathbf{C}_3)_{\mathrm{CCSD(T)}}$[c]	0.5	−12.8	−1.9	−4.7	−1.0	−11.0
$\tilde{E}^{\ddagger}(\mathbf{S})_{\mathrm{final\ estimate}}$	129.7	220.9	129.7	142.7	102.5	190.3
Difference to PBE	45.4	47.8	38.1	29.0	6.6	20.4
$\Delta E^{\ddagger}(\mathbf{S})_{\mathrm{ZPV}}$	−4.8	−14.7	−2.4	−11.4	−5.0	−6.7
$H^{\ddagger}(\mathbf{S})_{653} - E_0{}^{\ddagger}(\mathbf{S})_{\mathrm{PBE}}$[d]	−7.7	−0.4	−8.6	−2.5	−3.8	−1.9
$\Delta E^{\ddagger}(\mathbf{S})_{\mathrm{D//PBE}}$	−14.4	2.1	−7.5	−3.0	−22.7	−15.9
$E^{\ddagger}(\mathbf{S})_{\mathrm{PBE+D//PBE}}$	69.9	175.3	84.1	110.7	73.2	154.0
$\Delta E^{\ddagger}(\mathbf{C}_{16})^{\mathrm{DFT+D}}_{\mathrm{high}}$	56.0	62.7	53.9	51.6	35.1	42.2
$E^{\ddagger}(\mathrm{S})^{\mathrm{DFT+D}}_{\mathrm{final\ estimate}}$	127.3	227.7	136.7	151.2	107.5	195.5

[a]Energies as predicted using the parameters of Grimme (119). Zero-point vibrational energies and thermal contributions to adsorption enthalpies are also included. All energies are in kJ mol^{-1} (115).
[b]For 18T cluster.
[c]Difference between CCSD(T) and RI-MP2 energy barriers on a 3T cluster.
[d]Contribution to enthalpy at 653 K. $E_0{}^{\ddagger}(\mathbf{S})_{\mathrm{PBE}}$ is the ZPVE corrected energy barrier.

For benzene adsorption in H-ZSM-5, the most reliable experimental value for the enthalpy of adsorption is −63.6 kJ mol^{-1} (117). Other results range from −59.0 to −69.0 kJ mol^{-1}, indicating an uncertainty range of ± 5 kJ mol^{-1} (81, 115). The experimental enthalpy of adsorption for ethylbenzene [−87 kJ mol^{-1} (118)] is 23 kJ mol^{-1} more negative than that for benzene. The calculated adsorption enthalpies for ethene, benzene, and ethylbenzene are more negative by 8, 10–14, 14 and 23 kJ mol^{-1}, respectively, than the experimental values. This small (2–4 kJ mol^{-1} per CH_n unit) and systematic overestimation of the strength of the binding to the Brønsted acid site is ascribed to remaining uncertainties in the methodology. Compared with previous B3LYP T33 cluster results for ethene, benzene, and ethylbenzene (81), which were 3, 24, and 48 kJ mol^{-1}, respectively, too small (in absolute terms), the final estimated adsorption enthalpies represent a substantial improvement.

Table 3 shows the final estimate for intrinsic energy barriers that are obtained from the PBE energy barrier, the high-level corrections extrapolated to the periodic limit, the basis set limit corrections, and the CCSD(T) corrections. For the one-step scheme, the energy barrier is 129.7 kJ mol^{-1}, whereas for the two-step scheme, we obtained 129.7 kJ mol^{-1} for the first step and 102.5 kJ mol^{-1} for the second step. Whereas the energy barrier for the one-step scheme determined in the present study differs only slightly from that determined in our study ($E^{\ddagger}$ = 123.2 kJ mol^{-1}) (115), significant deviations for the two-step scheme were found. For the first step, the final estimate barrier is 24 kJ mol^{-1} higher, although it is 13 kJ mol^{-1} lower for the second step. In these calculations of energy barriers for the alkylation, the hybrid MP2:DFT results are affected by the same type of uncertainties as the calculations of adsorption energies. Therefore, an uncertainty range of ± 10 kJ mol^{-1} is expected.

As noted above, our original estimates of the apparent activation energy for benzene ethylation on H-ZSM-5 via the one-step mechanism was 15 kJ mol^{-1} too low relative to that reported experimentally. Comparison assuming dominance of the one-step mechanism is justified because

the experimental measurements were made with an excess of benzene, in which case all the active sites are saturated by the more strongly adsorbing benzene. Using the results of the improved calculations of the adsorption enthalpies for benzene (Reaction 2), coadsorption of ethene and benzene (Reaction 4), and the intrinsic activation energy for the one-step ethylation of benzene, we obtain an apparent activation energy of 74.4 kJ mol^{-1}, in reasonable agreement with the value obtained from the continuum model, 66.1 kJ mol^{-1}, and the experimental values, 58–76 kJ mol^{-1}.

CONCLUSIONS

The first part of this overview provides a concise overview of DFT methods, which are the most widely used family of quantum mechanical methods for modeling complex catalytic systems. Progress in the development of functionals has been sufficient to permit reliable calculations on a broad range of systems. New-generation functionals appear to offer useful advances over established functionals from the 1990s, although open challenges and limitations remain. The exploration of these quantum-mechanically derived potential energy surfaces, both by local optimization and path-finding methods that connect reactants and products, are then discussed. Local optimization methods are mature and efficient in terms of computer time, though user insight is needed to search for appropriate structures. Path-finding methods are far more computationally expensive at present, but they can reduce the human effort needed to locate relevant reaction coordinates.

The four illustrations presented here demonstrate the wealth of chemical information that can be gained from electronic-structure calculations for both homogeneously and heterogeneously catalyzed reactions. These include the structure of adsorbed and transition states, the enthalpy of adsorption for reactants and products, the activation energies for elementary reactions, and vibrational frequencies for adsorbed species. Such calculations allow for a rational explanation of solvent effects on the dissociation of catalyst precursors, the effects of ligand composition on the kinetics of homogeneously catalyzed reactions, and the rate parameters for heterogeneously catalyzed reactions. Electronic-structure calculations can also be used to confirm the structure of catalytically active centers inferred from experimental observation and in combination with absolute-rate theory to determine rate parameters for elementary reactions and the overall rates of reaction. The latter calculations agree well in many instances with experimental observation and can be used to explore the consequence of changing the composition and structure of catalytically active sites.

DISCLOSURE STATEMENT

The authors are not aware of any affiliations, memberships, funding, or financial holdings that might be perceived as affecting the objectivity of this review.

ACKNOWLEDGMENTS

This work was supported by the Director, Office of Energy Research, Office of Basic Energy Sciences, Chemical Science Division, of the U.S. Department of Energy under contract number DE-AC03-76SF00098; the Methane Conversion Cooperative funded by British Petroleum; and Chevron Energy and Technology Company.

LITERATURE CITED

1. Lewis GN. 1933. The chemical bond. *J. Chem. Phys.* 1:17–28
2. Head-Gordon M, Artacho E. 2008. Chemistry on the computer. *Phys. Today* 61:58–63
3. Pople JA. 1999. Nobel lecture: quantum chemical models. *Rev. Mod. Phys.* 71:1267–74
4. Hohenberg P, Kohn W. 1964. Inhomogeneous electron gas. *Phys. Rev. B* 136:B864–71
5. Levy M. 1979. Universal variational functionals of electron-densities, first-order density-matrices, and natural spin-orbitals and solution of the v-representability problem. *Proc. Natl. Acad. Sci. USA* 76:6062–65
6. Chai JD, Ligneres VL, Ho G, Carter EA, Weeks JD. 2009. Orbital-free density functional theory: linear scaling methods for kinetic potentials, and applications to solid Al and Si. *Chem. Phys. Lett.* 473:263–67
7. Kohn W, Sham LJ. 1965. Self-consistent equations including exchange and correlation effects. *Phys. Rev.* 140:A1133–38
8. Perdew JP, Ruzsinszky A, Constantin LA, Sun JW, Csonka GI. 2009. Some fundamental issues in ground-state density functional theory: a guide for the perplexed. *J. Chem. Theor. Comput.* 5:902–8
9. Perdew JP, Burke K, Ernzerhof M. 1997. Generalized gradient approximation made simple. *Phys. Rev. Lett.* 78:1396–96
10. Becke AD. 1988. Density-functional exchange-energy approximation with correct asymptotic-behavior. *Phys. Rev. A* 38:3098–100
11. Lee CT, Yang WT, Parr RG. 1988. Development of the Colle-Salvetti correlation-energy formula into a functional of the electron-density. *Phys. Rev. B* 37:785–89
12. Becke AD. 1993. Density-functional thermochemistry. 3. The role of exact exchange. *J. Chem. Phys.* 98:5648–52
13. Hertwig RH, Koch W. 1997. On the parameterization of the local correlation functional. What is Becke-3-LYP? *Chem. Phys. Lett.* 268:345–51
14. Kummel S, Kronik L. 2008. Orbital-dependent density functionals: theory and applications. *Rev. Mod. Phys.* 80:3–60
15. Cohen AJ, Mori-Sanchez P, Yang WT. 2008. Insights into current limitations of density functional theory. *Science* 321:792–94
16. Grafenstein J, Kraka E, Cremer D. 2004. The impact of the self-interaction error on the density functional theory description of dissociating radical cations: ionic and covalent dissociation limits. *J. Chem. Phys.* 120:524–39
17. Johnson BG, Gonzales CA, Gill PMW, Pople JA. 1994. A density-functional study of the simplest hydrogen abstraction reaction—effect of self-interaction correction. *Chem. Phys. Lett.* 221:100–108
18. Leininger T, Stoll H, Werner HJ, Savin A. 1997. Combining long-range configuration interaction with short-range density functionals. *Chem. Phys. Lett.* 275:151–60
19. Gill PMW, Adamson RD, Pople JA. 1996. Coulomb-attenuated exchange energy density functionals. *Mol. Phys.* 88:1005–9
20. Iikura H, Tsuneda T, Yanai T, Hirao K. 2001. A long-range correction scheme for generalized-gradient-approximation exchange functionals. *J. Chem. Phys.* 115:3540–44
21. Kristyan S, Pulay P. 1994. Can (semi)local density-functional theory account for the London dispersion forces. *Chem. Phys. Lett.* 229:175–80
22. Wu Q, Yang WT. 2002. Empirical correction to density functional theory for Van der Waals interactions. *J. Chem. Phys.* 116:515–24
23. Antony J, Grimme S. 2006. Density functional theory including dispersion corrections for intermolecular interactions in a large benchmark set of biologically relevant molecules. *Phys. Chem. Chem. Phys.* 8:5287–93
24. Lee K, Murray ED, Kong LZ, Lundqvist BI, Langreth DC. 2010. Higher-accuracy Van der Waals density functional. *Phys. Rev. B* 82:081101
25. Vydrov OA, Van Voorhis T. 2010. Dispersion interactions from a local polarizability model. *Phys. Rev. A* 81:062708
26. Schwabe T, Grimme S. 2007. Double-hybrid density functionals with long-range dispersion corrections: higher accuracy and extended applicability. *Phys. Chem. Chem. Phys.* 9:3397–406

27. Mori-Sanchez P, Cohen AJ, Yang WT. 2009. Discontinuous nature of the exchange-correlation functional in strongly correlated systems. *Phys. Rev. Lett.* 102:066403
28. Isobe H, Shoji M, Koizumi K, Kitagawa Y, Yamanaka S, et al. 2005. Electronic and spin structures of manganese clusters in the photosynthesis II system. *Polyhedron* 24:2767–77
29. Kurzweil Y, Lawler KV, Head-Gordon M. 2009. Analysis of multi-configuration density functional theory methods: theory and model application to bond-breaking. *Mol. Phys.* 107:2103–10
30. Chai JD, Head-Gordon M. 2008. Systematic optimization of long-range corrected hybrid density functionals. *J. Chem. Phys.* 128:084106
31. Becke AD. 1997. Density-functional thermochemistry. 5. Systematic optimization of exchange-correlation functionals. *J. Chem. Phys.* 107:8554–60
32. Chai JD, Head-Gordon M. 2008. Long-range corrected hybrid density functionals with damped atom-atom dispersion corrections. *Phys. Chem. Chem. Phys.* 10:6615–20
33. Koch W, Holthausen MC. 2001. *A Chemist's Guide to Density Functional Theory*. Weinheim: Wiley-VCH
34. Schmider HL, Becke AD. 1998. Density functionals from the extended G2 test set: second-order gradient corrections. *J. Chem. Phys.* 109:8188–99
35. Zhao Y, Truhlar DG. 2008. The M06 suite of density functionals for main group thermochemistry, thermochemical kinetics, noncovalent interactions, excited states, and transition elements: two new functionals and systematic testing of four M06-class functionals and 12 other functionals. *Theor. Chem. Acc.* 120:215–41
36. Yang K, Zheng JJ, Zhao Y, Truhlar DG. 2010. Tests of the RPBE, revPBE, tau-HCTHhyb, omega B97X-D, and MOHLYP density functional approximations and 29 others against representative databases for diverse bond energies and barrier heights in catalysis. *J. Chem. Phys.* 132:164117
37. Schlegel HB. 2003. Exploring potential energy surfaces for chemical reactions: an overview of some practical methods. *J. Comput. Chem.* 24:1514–27
38. E W, Vanden-Eijnden E. 2010. Transition-path theory and path-finding algorithms for the study of rare events. *Annu. Rev. Phys. Chem.* 61:391–420
39. Bakken V, Helgaker T. 2002. The efficient optimization of molecular geometries using redundant internal coordinates. *J. Chem. Phys.* 117:9160–74
40. Baker J, Kessi A, Delley B. 1996. The generation and use of delocalized internal coordinates in geometry optimization. *J. Chem. Phys.* 105:192–212
41. Baker J. 1986. An algorithm for the location of transition-states. *J. Comput. Chem.* 7:385–95
42. Heyden A, Bell AT, Keil FJ. 2005. Efficient methods for finding transition states in chemical reactions: comparison of improved dimer method and partitioned rational function optimization method. *J. Chem. Phys.* 123:224101
43. Weinan EN, Ren WQ, Vanden-Eijnden E. 2002. String method for the study of rare events. *Phys. Rev. B* 66:052301
44. Peters B, Heyden A, Bell AT, Chakraborty A. 2004. A growing string method for determining transition states: comparison to the nudged elastic band and string methods. *J. Chem. Phys.* 120:7877–86
45. Fukui K. 1981. The path of chemical-reactions—the IRC approach. *Acc. Chem. Res.* 14:363–68
46. Henkelman G, Uberuaga BP, Jonsson H. 2000. A climbing image nudged elastic band method for finding saddle points and minimum energy paths. *J. Chem. Phys.* 113:9901–4
47. Goodrow A, Bell AT, Head-Gordon M. 2008. Development and application of a hybrid method involving interpolation and ab initio calculations for the determination of transition states. *J. Chem. Phys.* 129:174109
48. Goodrow A, Bell AT, Head-Gordon M. 2009. Transition state-finding strategies for use with the growing string method. *J. Chem. Phys.* 130:244108
49. Stephenson NA, Bell AT. 2005. A study of the mechanism and kinetics of cyclooctene epoxidation catalyzed by iron(III) tetrakispentafluorophenyl porphyrin. *J. Am. Chem. Soc.* 127:8635–43
50. Stephenson NA, Bell AT. 2006. Effects of methanol on the thermodynamics of iron(III) [tetrakis(pentafluorophenyl)] porphyrin chloride dissociation and the creation of catalytically active species for the epoxidation of cyclooctene. *Inorg. Chem.* 45:5591–99

51. Khaliullin RZ, Head-Gordon M, Bell AT. 2007. Theoretical study of solvent effects on the thermodynamics of iron(III) [tetrakis(pentafluorophenyl)]porphyrin chloride dissociation. *J. Phys. Chem. B* 111:10992–98
52. Tomasi J, Persico M. 1994. Molecular interactions in solution—an overview of methods based on continuous distribution of the solvent. *Chem. Rev.* 94:2027–94
53. Cramer CJ, Truhlar DG. 1999. Implicit solvation models: equilibria, structure, spectra, and dynamics. *Chem. Rev.* 99:2161–200
54. Tomasi J, Mennucci B, Cammi R. 2005. Quantum mechanical continuum solvation models. *Chem. Rev.* 105:2999–3093
55. Paulaitis ME, Pratt LR. 2002. Quantum mechanical continuum solvation models. *Adv. Protein Chem.* 62:283–310
56. Chipman DM. 2002. Comparison of solvent reaction field representations. *Theor. Chem. Acc.* 107:80–89
57. Taniguchi Y, Yamaoka Y, Nakata K, Takaki K, Fujiwara Y. 1995. Palladium(II) catalyzed carboxylation of aromatic-compounds with CO under very mild conditions. *Chem. Lett.* 5:345–46
58. Kalinovskii IO, Pogorelov VV, Gelbshtein AI, Akhemtov NG. 2001. Oxidative carbonylation of aromatic hydrocarbons in the system containing Pd or Rh compound, trifluoroacetic acid and its anhydride, and MnO_2 or Mn_2O_3. *Russ. J. Gen. Chem.* 71:1463–66
59. Zakzeski J, Behn A, Head-Gordon M, Bell AT. 2009. Effect of ligand composition on the oxidative carbonylation of toluene to toluic acid catalyzed by Rh(III) complexes. *J. Am. Chem. Soc.* 131:11098–105
60. Zakzeski J, Bell AT. 2009. Oxidative carbonylation of benzotrifluoride to form trifluoromethylbenzoic acid. *J. Mol. Catal. A Chem.* 302:59–67
61. Zakzeski JJ, Bell AT. 2007. Oxidative carbonylation of toluene to p-toluic acid catalyzed by rhodium in the presence of vanadium and oxygen. *J. Mol. Catal. A Chem.* 276:8–16
62. Zheng XB, Bell AT. 2008. Theoretical analysis of the mechanism for the oxidative carbonylation of toluene to p-toluic acid by rhodium complexes. *J. Phys. Chem. C* 112:2129–36
63. Zakzeski JJ, Burton S, Behn A, Head-Gordon M, Bell AT. 2009. Spectroscopic investigation of the species involved in the rhodium-catalyzed oxidative carbonylation of toluene to toluic acid. *Phys. Chem. Chem. Phys.* 11:9903–11
64. Baltes M, Cassiers K, Van Der Voort P, Weckhuysen BM, Schoonheydt RA, Vansant EF. 2001. MCM-48-supported vanadium oxide catalysts, prepared by the molecular designed dispersion of $VO(acac)_2$: a detailed study of the highly reactive MCM-48 surface and the structure and activity of the deposited VO_x. *J. Catal.* 197:160–71
65. Lim SY, Haller GL. 1999. Gas phase methanol oxidation on V-MCM-41. *Appl. Catal. A Genl.* 188:277–86
66. Bronkema J, Bell AT. 2007. Mechanistic studies of methanol oxidation to formaldehyde on isolated vanadate sites supported on MCM-48. *J. Phys. Chem. C* 111:420–30
67. Burcham LJ, Wachs IE. 1999. The origin of the support effect in supported metal oxide catalysts: in situ infrared and kinetic studies during methanol oxidation. *Catal. Today* 49:467–84
68. Burcham LJ, Deo G, Gao X, Wachs IE. 2000. In situ IR, Raman, and UV-Vis DRS spectroscopy of supported vanadium oxide catalysts during methanol oxidation. *Topics Catal.* 11/12:85–100
69. Feng T, Vohs JM. 2005. Temperature-programmed desorption study of the selective oxidation of alcohols on silica-supported vanadium oxide. *J. Phys. Chem. B* 109:2120–27
70. Burcham LJ, Briand LE, Wachs IE. 2001. Quantification of active sites for the determination of methanol oxidation turn-over frequencies using methanol chemisorption and in situ infrared techniques. 1. Supported metal oxide catalysts. *Langmuir* 17:6164–74
71. Burcham LJ, Badlani M, Wachs IE. 2001. The origin of the ligand effect in metal oxide catalysts: Novel fixed-bed in situ infrared and kinetic studies during methanol oxidation. *J. Catal.* 203:104–21
72. Deo G, Wachs IE. 1994. Reactivity of supported vanadium-oxide catalysts: The partial oxidation of methanol. *J. Catal.* 146:323–34
73. Koningsberger DC, Prins R. 1988. *X-Ray Absorption: Principles, Applications, Techniques of EXAFS, SEXAFS and XANES*. New York: Wiley-Interscience
74. Khaliullin RZ, Bell AT. 2002. A density functional theory study of the oxidation of methanol to formaldehyde over vanadia supported on silica, titania, and zirconia. *J. Phys. Chem. B* 106:7832–38

75. Döbler J, Pritzsche M, Sauer J. 2005. Oxidation of methanol to formaldehyde on supported vanadium oxide catalysts compared to gas phase molecules. *J. Am. Chem. Soc.* 127:10861
76. Goodrow A, Bell AT. 2007. A theoretical investigation of the selective oxidation of methanol to formaldehyde on isolated vanadate species supported on silica. *J. Phys. Chem. C* 111:14753–61
77. Jaguar. 2005. Version 6.5. New York: Schrodinger
78. Scott AP, Random L. 1996. Harmonic vibrational frequencies: an evaluation of Hartree-Fock, Moller-Plesset, quadratic configuration interaction, density functional theory, and semiempirical scale factors. *J. Phys. Chem.* 100:16502–13
79. Peng C, Ayala PY, Schlegel HB, Frisch MJ. 1996. Using redundant internal coordinates to optimize equilibrium geometries and transition states. *J. Comp. Chem.* 17:49–56
80. Peng C, Schlegel HB. 1993. Combing synchronous transit and quasi-Newton methods to find transition states. *Israel J. Chem.* 33:449–54
81. Noodleman L. 1981. Valence bond description of anti-ferromagnetic coupling in transition-metal dimers. *J. Chem. Phys.* 74:5737–43
82. Caballol R, Castell O, Illas F, Moreira I de PR, Malrieu JP. 1997. Remarks on the proper use of the broken symmetry approach to magnetic coupling. *J. Phys. Chem. A* 101:7860–66
83. Goodrow A, Bell AT, Head-Gordon M. 2009. Are spin-forbidden crossings a bottleneck in methanol oxidation? *J. Phys. Chem. C Lett.* 113:19361–64
84. Ochterski JW. 2000. *Thermochemistry in Gaussian*. **http://www.gaussian.com/g_whitepap/thermo.htm**
85. McQuarrie DA. 2000. *Statistical Mechanics*. Sausalito: Univ. Sci. Books
86. Chandler D. 1987. *Introduction to Modern Statistical Mechanics*. New York: Oxford Univ. Press
87. Atkins P, dePaula J. 2002. *Physical Chemistry*. New York: WH Freeman. 7th ed.
88. Hill TL. 1986. *An Introduction to Statistical Thermodynamics*. New York: Dover Publ.
89. Wong GS, Concepcion MR, Vohs JM. 2002. Oxidation of methanol to formaldehyde on vanadia films supported on CeO_2(111). *J. Phys. Chem. B* 106:6451–55
90. Masel RI. 2001. *Chemical Kinetics and Catalysis*. New York: Wiley-Interscience
91. Moulijn JA, Makkee M, van Diepen A. 2001. *Chemical Process Technology*. Chichester: Wiley
92. Degnan TF, Morris Smith C, Venkat CR. 2001. Alkylation of aromatics with ethylene and propylene: recent developments in commercial processes. *Appl. Catal. A* 221:283–94
93. Dwyer FG, Lewis PJ, Schneider FH. 1976. Efficient, nonpolluting ethylbenzene process. *Chem. Eng.* 83:90–91
94. Haag WO, Olson DH, Weisz PB. 1984. Shape-selective catalysis in aromatics processing. In *Chemistry for the Future*, Proc. 29th IUPAC Congr., ed. H Grünewald, p. 327. Oxford: Pergamon
95. Caeiro G, Carvalho RH, Wang X, Lemos MANDA, Lemos F, et al. 2006. Activation of C_2-C_4 alkanes over acid and bifunctional zeolite catalysts. *J. Mol. Catal. A* 255:131–58
96. Smirniotis PG, Ruckenstein E. 1995. Alkylation of benzene or toluene with MeOH or C_2H_4 over ZSM-5 or β zeolite: effect of the zeolite pore openings and of the hydrocarbons involved on the mechanism of alkylation. *Ind. Eng. Chem. Res.* 34:1517–28
97. You H, Long W, Pan Y. 2006. The mechanism and kinetics for the alkylation of benzene with ethylene. *Petroleum Sci. Technol.* 24:1079–88
98. Vos AM, Schoonheydt RA, De Proft F, Geerlings P. 2003. Reactivity descriptors and rate constants for acid zeolite catalyzed ethylation and isopropylation of benzene. *J. Phys. Chem. B* 107:2001–8
99. Arstad B, Kolboe S, Swang O. 2004. Theoretical investigation of arene alkylation by ethane and propene over acidic zeolites. *J. Phys. Chem. B* 108:2300–8
100. Namuangruk S, Pantu P, Limtrakul J. 2004. Alkylation of benzene with ethylene over faujasite zeolite investigated by the ONIOM method. *J. Catal.* 225:523–30
101. Humbel S, Sieber S, Morokuma K. 1996. The IMOMO method: integration of different levels of molecular orbital approximations for geometry optimizations of large systems. Test for *n*-butane conformation and S_n2 reaction: $RCl+Cl^-$. *J. Chem. Phys.* 105:1959–67
102. Hansen N, Bruggemann T, Bell AT, Keil FJ. 2008. Theoretical investigation of benzene alkylation with ethene over H-ZSM-5 zeolite. *J. Phys. Chem. C* 112:15402–11
103. Olson DH, Kokotailo GT, Lawton SL, Meier WM. 1981. Crystal structure and structure-related properties of ZSM-5. *J. Phys. Chem.* 85:2238–43

104. Hansen N, Krishna R, van Baten JM, Bell AT, Keil FJ. 2009. Analysis of diffusion limitation in the alkylation of benzene over H-ZSM-5 by combining quantum chemical calculations, molecular simulations, and a continuum approach. *J. Phys. Chem. C* 113:235–46
105. Christensen CH, Johannsen K, Schmidt I, Christensen CH. 2003. Catalytic benzene alkylation over mesoporous zeolite single crystals: Improving activity and selectivity with a new family of porous materials. *J. Am. Chem. Soc.* 125:13370–71
106. Wesolowski TA, Parisel O, Ellinger Y, Weber J. 1997. Comparative study of benzene···X (X = O_2, N_2, CO) complexes using density functional theory: the importance of an accurate exchange-correlation energy density at high reduced density gradients. *J. Phys. Chem. A* 101:7818–25
107. Zhang Y, Pan W, Yang W. 1997. Describing van der Waals interaction in diatomic molecules with generalized gradient approximations: the role of the exchange functional. *J. Chem. Phys.* 107:7921–25
108. Gritsenko OV, Ensing B, Schipper PRT, Baerends EJ. 2000. Comparison of the accurate Kohn-Sham solution with the generalized gradient approximations GGAs for the S_N2 reactions $F^- + CH_3F \rightarrow FCH_3 + F^-$: a qualitative rule to predict success or failure of GGAs. *J. Phys. Chem. A* 104:8558–65
109. Porezag D, Pederson MR. 1995. Density functional based studies of transition states and barriers for hydrogen exchange and abstraction reactions. *J. Chem. Phys.* 102:9345–49
110. Tuma C, Sauer J. 2006. Treating dispersion effects in extended systems by hybrid MP2:DFT calculations—protonation of isobutene in zeolite ferrierite. *Phys. Chem. Chem. Phys.* 8:3955–65
111. Kerber T, Sierka M, Sauer J. 2008. Application of semiempirical long-range dispersion corrections to periodic systems in density functional theory. *J. Comput. Chem.* 29:2088–97
112. Zhao Y, Truhlar DG. 2005. Design of density functionals that are broadly accurate for thermochemistry, thermochemical kinetics, and nonbonded interactions. *J. Phys. Chem. A* 109:5656–67
113. Zhao Y, Truhlar DG. 2008. Density functionals with broad applicability in chemistry. *Acc. Chem. Res.* 41:157–67
114. Tuma C, Sauer J. 2004. A hybrid MP2/planewave-DFT scheme for large chemical systems: proton jumps in zeolites. *Chem. Phys. Lett.* 387:388–94
115. Hansen N, Kerber T, Sauer J, Bell AT, Keil FJ. 2010. Quantum chemical modeling of benzene ethylation over H-ZSM-5 approaching chemical accuracy: a hybrid MP2:DFT study. *J. Am. Chem. Soc.* 132:115225–38
116. Svelle S, Tuma C, Rozanska X, Kerber T, Sauer J. 2009. Quantum chemical modeling of zeolite-catalyzed methylation reactions: Toward chemical accuracy for barriers. *J. Am. Chem. Soc.* 131:816–25
117. Thamm H, Jerschkewitz H-G, Stach H. 1988. Calorimetric study on the state of benzene and cyclopentane sorbed on H-ZSM-5 with different Si/Al ratios. *Zeolites* 8:151–53
118. Niessen W, Karge HG, Jozefowicz L. 1993. Thermodynamic and kinetic data of sorption in zeolites determined by FTIR. *Stud. Surf. Sci. Catal.* 80:475–81
119. Grimme J. 2006. Semiempirical GGA-type density functional constructed with a long-range dispersion correction. *J. Comput. Chem.* 27:1787–99

Annual Review of Chemical and Biomolecular Engineering

Volume 2, 2011

Contents